Soft Matter

Quantifying memory: Detection of focal conic domain rearrangement across a phase transition

Journal:	*Soft Matter*
Manuscript ID	SM-ART-08-2024-000940.R2
Article Type:	Paper
Date Submitted by the Author:	22-Jan-2025
Complete List of Authors:	Hare, Sean; Johns Hopkins University, Physics and Astronomy de la Vega, Alexander; Johns Hopkins University, Physics and Astronomy; UC Riverside Serra, Francesca; University of Southern Denmark, Physics, Chemistry and Pharmacy; Johns Hopkins University, Physics and Astronomy

Soft Matter

ARTICLE TYPE

Cite this: DOI: 00.0000/xxxxxxxxxx

Quantifying memory: Detection of focal conic domain rearrangement across a phase transition†

Sean Hare,[a] Alexander de la Vega,[a] and Francesca Serra[a,b]

Received Date
Accepted Date

DOI: 00.0000/xxxxxxxxxx

The behavior of topological defects near phase transition in liquid crystals has stimulated research in recent years, which has shown that a certain amount of "memory" is retained when a defect characteristic of a liquid crystal phase turns into a defect belonging to a different phase. We aim to quantify this "memory effect" at the transition between smectic-A and nematic liquid crystal phases using as testbed focal conic domains in topographic confinement. These geometric defects, which spontaneously form in the smectic-A phase, disappear above the phase transition. However, we show that when the system is cooled back into the smectic phase, the defects tend to reform in their original location and that this behavior depends on the temperature at which they are heated, suggesting that the system retains temperature-dependent information about defect configurations across the phase transition despite the difference in the molecular alignment in the two phases.

1 Introduction

In the last few decades, research has explored uses of liquid crystals (LCs) beyond displays, for example as storage devices or bistable displays. These applications rely on the LC system having "memory", i.e. the ability to "remember" information about the history of transformations they have undergone. This memory is intrinsic to the LC alignment or mediated by a secondary surface/network that controls LC alignment. Diverse systems with electro-optic [1–4], dielectric [5,6] and electromechanical [7] memory have demonstrated potential use as dynamic or non-volatile memory storage devices. Memory in LCs has been shown in surface-memory effects, where bulk alignment can be "remembered" through surface interactions [8–10]. Bistable nematic devices such as ZBD displays [11] can be described as an example of bulk memory [12–14] and recently it has been shown that shear-induced alignment can be retained in discotic LCs, after the stimulus is finished [15].

In some of the previous examples, the memory is mediated by topological defects, the locations where the LC order is not defined. For example, nematics confined in porous structures lack a well-defined ground state, with a high density of topological defect lines that exist in metastable configurations [13,16]. An external field can break the symmetry and favor a defect configuration that results in a net molecular alignment in the direction of the field–alignment, which is retained after the removal of the field [14,16,17]. Defects also play a role in active nematic memory effects, where their movement can leave persistent trails in the director field [18].

We focus now on the case where the system has memory of its thermal history. Memory across a phase transition has been observed and analyzed in thin-film nematics with hybrid anchoring at the smectic-A–nematic transition [19,20]. In this system, boojum defects in the nematic phase spontaneously form a lattice, and the geometry of this lattice is imprinted on the orientation (tilt) of smectic focal conic domains (FCDs) [19]. Re-heating the system recovers the boojum lattice. The "memory" here is mediated by the molecular alignment, which is similar for FCDs and one particular type of boojums. However, cooling the system significantly below the nematic-smectic transition temperature transforms all FCDs into toric FCDs, and the original nematic configuration is forgotten.

Our own previous research has also shown an example of defects undergoing a transformation across the smectic-A*-cholesteric phase transition [21] and keeping their location. Both the smectic and the cholesteric phase have stable 3D geometric defects of zero total topological charge, but characterized by a very different molecular alignment. However, both contain a disclination with +1 winding number. We have shown that the location of the defects tends to remain the same across the phase transition from smectic to cholesteric and vice-versa and we have hypothesized that the +1 disclination mediates the memory. All these data point to the existence of a relationship between defects, memory, and phase transition.

The goal of this research is to identify a system where we can extract a quantitative measurement of memory, and in particular

[a] Department of Physics and Astronomy, Johns Hopkins University, Baltimore, MD 21218.
[b] Department of Physics, Chemistry and Pharmacy, University of Southern Denmark, 5230 Odense, Denmark.

† Electronic Supplemental Information (ESI) available: [details of any supplemental information available should be included here]. See DOI: 10.1039/cXsm00000x/

the amount of change, or lack thereof, in the defects' locations after the system has undergone a phase transition. In this paper, we define geometric memory as the ability to reconstitute geometric defects (the FCDs) in the smectic-A phase after the system has been brought across the nematic transition. For our quantitative analysis, we specifically study the case of FCDs confined into regular arrays.

1.1 Focal Conic Domain (FCD) Arrays

FCDs are a type of defect that spontaneously form in smectic-A liquid crystals in the presence of hybrid anchoring conditions. In FCDs, smectic layers curve around two singular, conjugated lines—one branch of a hyperbola, and an ellipse—which together we treat as a single defect object with zero total topological charge. In a flat film FCDs will pack in a space-filling hexagonal arrangement [22–24]. However, it is possible to alter the spontaneous FCD packing in various ways, for example with the use of surface patterning [25–27], curved surfaces [28,29], curved air-liquid interfaces [30], micropillars [31], or other confined geometries [23,32] that direct their self-assembly. Directed self-assembly of FCDs has great potential use, as smectics and FCDs have been explored as micro-lens arrays [21,30,33] and for colloid and nanoparticle assembly [34–37].

In this paper we expand upon these methods of positional control using curved microchannel walls. We utilize geometric confinement to form large FCDs in micro-channel pockets and we explain their behavior when subjected to annealing at various temperatures. Finally we propose a way to use the conditional probability of forming FCDs repeatedly at the same locations as a quantitative measurement of the system memory. We demonstrate that the extent to which an array of focal conic domains can be recovered depends on the maximum heating temperature.

In addition to our research of memory and defect arrays, we demonstrate the use of automatic image segmentation for FCD detection. Automated image analysis is a rapidly developing field of research in LCs, with machine learning models employed in recent years for the detection and tracking of topological defects in simulated nematic textures [38,39], cross-polarized images of smectic-C films [40,41], active nematics [42], or individual models that can characterize defects across diverse nematic textures [43]. Models have also been successful in detecting islands and bubbles in smectic-A films [44], detecting and classifying nematic defects in confluent cell layers [45], and classifying images of different LC phases [39,46,47].

Unlike the majority of existing research, ours does not employ neural networks and instead uses algorithms modifiable with user-defined parameters, a technique recently employed in smectic-A/smectic-B texture classification [48]. In our case, we demonstrate a method to identify and classify individual smectic-A FCDs with the use of image segmentation—a commonly employed tool in galaxy detection [49] and biological tissue analysis. The use of this technique, as we demonstrate here, allows us to make automatic and unbiased defect detection and opens our system to statistical analyses.

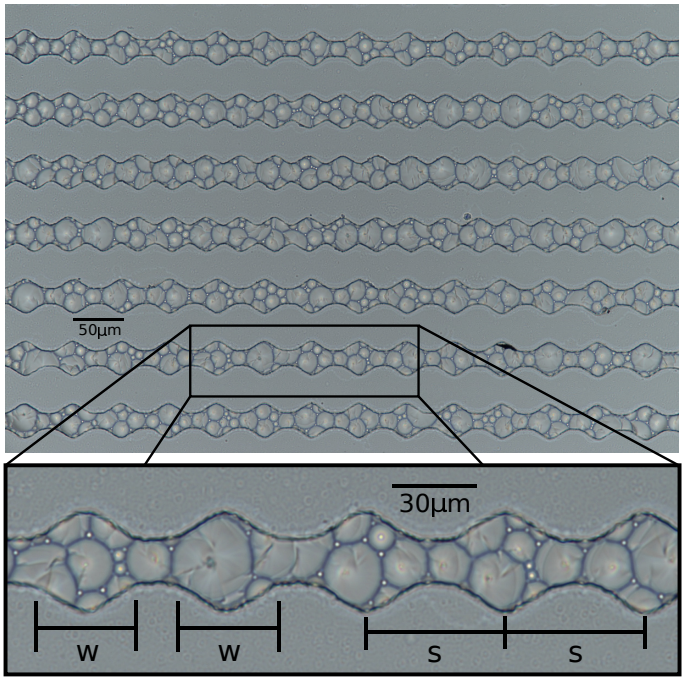

Fig. 1 Curved microchannels filled with 8CB in the smectic phase, forming focal conic domains. Pocket indendation width (w) and spacing between pockets (s) for a given channel are indicated.

2 Materials and Methods

2.1 Sample Preparation

We designed a photomask with microchannel walls that have periodic indentations across from each other forming roughly circular repeating pockets, where large FCDs sometimes spontaneously form. The design is shown in Fig. 1. The narrowest part of the channels tested ranged from 15–20μm, and the widest part was approximately 36μm wide. Microchannel walls had a measured height of approximately 14–15μm. Samples tested had a spacing (s) between pockets of 36–50μm. Pocket indentation width (w) was 24–36μm. Channels are classified into distinct 'geometries' corresponding to a given combination of pocket indentation width and pocket spacing.

The microchannels were fabricated using photolithography with SU-8 2010 negative photoresist on 1mm pre-cleaned glass slides, using a mylar mask to create our design. Spin-coating and baking was done according to the manufacturer's processing guidelines [50], with the additional step of hard baking at 200C for 10-15 minutes for surface annealing to provide extra temperature stability (given the nature of the experiment).

Microchannels were filled with 4'-octyl-4 biphenylcarbonitrile (8CB, Nematel Gmbh) smectic liquid crystal, with a smectic–nematic phase transition at 33.3C and nematic–isotropic phase transition at 40.8C. Microchannels were open to air on the top allowing for homeotropic anchoring of the LC. The walls of the SU-8 microchannels, without additional treatment, give degenerate planar anchoring, providing necessary hybrid anchoring for spontaneous FCD formation. Channels were filled by pipetting a small drop of 8CB on a flat portion of the sample next to the microchannels, and allowing the channels to fill completely by

capillary action while in the isotropic phase. This resulted in a LC film height 1-2μm below the tallest part of the microchannel (estimated using laser-scanning microscopy in the smectic phase). Afterwards, the droplet was blown off to the side with clean air, leaving a small reservoir of 8CB to ensure that channels were always maximally filled. Samples were left at isotropic phase above 50C for at least one hour and left at smectic phase overnight after filling before use in experiments. Samples were always left at the isotropic phase for at least 1 hour immediately before starting experiments, and left to relax at room temperature (in smectic phase) for 20-30 minutes immediately before beginning temperature ramps.

2.2 Temperature Protocol

Heating was controlled by a pre-programmed Instec mK2000 temperature controller and HCS302 heating stage consisting on a metal plate on which the sample sat directly, and an enclosure to improve uniformity. The temperature control stage was connected to an ice-water bath connected to a tube surrounding the sample holder. A small temperature gradient was present from the bottom to the top of the glass, as well as from the side to the center. By measuring the nematic-isotropic transition temperature and comparing it to literature, we estimated this to be 0.2C, as our measurements of nematic-isotropic transition gave 46.6C as the transition temperature. We should remark also that we took as reference temperature for the smectic-nematic transition the temperature at which we began to observe a significant rearrangement of the focal conic domains. This is about 0.2 degrees below the real smectic-nematic transition. By taking this temperature as reference, we could be sure than below this temperature the rearrangements were small. In this work, all the temperatures we refer to are those measured by our apparatus, without corrections.

In order to measure geometric memory of defects, we subjected samples to a series of controlled temperature ramps and studied the resulting FCD patterns in the smectic phase. A single temperature cycle (shown in Fig. 2.) contains the following steps:

1. The sample is heated to 41.6C—at least one degree above the measured nematic-isotropic phase transition (40.6C).
2. The sample is cooled rapidly into the nematic phase and towards the smectic phase, with the cooling rate decreasing step-wise as it approaches.
3. When the sample is 0.5-0.6C above the nematic-smectic phase transition (33.1C), the cooling rate is reduced to 0.05C/min to allow for relaxation (since the largest amount of rearrangement tends to occur in this temperature range).
4. The sample is then cooled to 32C (1C below smectic transition) to halt smectic relaxation as much as possible, and left for 6 minutes to allow for an automated image capture (which occurs every 5 minutes).
5. The sample is heated back to a desired temperature T_H (the 'heating' temperature). This value is varied in successive ramps.
6. The sample is cooled back in identical fashion to steps 2-4.

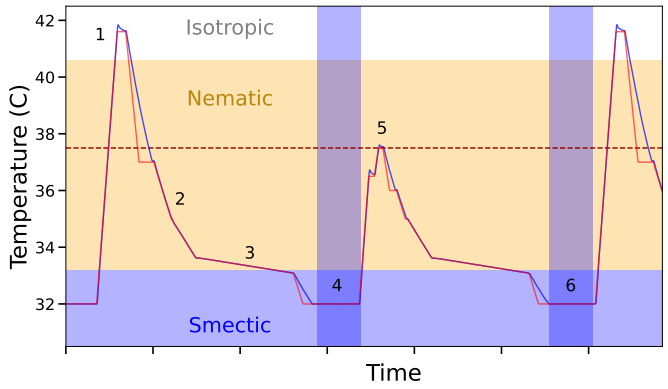

Fig. 2 An example of a typical programmed temperature cycle used in experiments. The ticks in the x-axis indicate 10-minute intervals. Red and blue plots represent TT and TC (heating stage transmitter and controller temperatures) respectively. The red horizontal dashed line (step 5) represents T_H, the heating temperature of this particular cycle. Images were taken in the smectic phase (blue vertical shaded regions; steps 4 and 6), and the cycle is repeated for a new T_H (not shown). We compare image of FCDs taken step 4 with the corresponding FCDs in step 6.

7. Steps 5-6 are repeated a desired amount of times (or not repeated at all).

In order to study the effects of heating on our system, the smectic images taken at step 4 and 6 (before and after heating to T_H) were compared. This direct comparison simply tells us how much heating the sample to T_H affects reconfiguration of FCDs.

We need to add some notes about our choice of parameters. First, the 0.05C/min cooling rate (step 3) results in a thirty minute cooling cycle from isotropic to smectic (steps 2–4). This cooling rate was chosen to be sufficiently slow to allow for the relaxation of smectic LCs near the phase transition. In fact, if the cooling rate increases, the total number of observed large FCDs decreases significantly, making any further analysis more difficult. In order to standardize our analysis (with respect to the variable T_H), we kept this cooling rate as a fixed variable throughout all experiments.

Morever, while we observe rearrangements in the FCDs upon further lowering the temperature below 32C, these rearrangements are very small to what happens within one degree from the phase transition temperature. This is especially true for the large FCDs on which we focus our research – if they form near the phase transition, they do not change at lower temperature. For this reason we choose 32C as lower temperature limit.

An additional note is that for data taken specifically at the lowest temperature, T_H=32C, steps 5–6 were skipped. Instead, the sample was left at 32C for thirty minutes (the approximate time steps 5–6 would otherwise take) and smectic images were taken before and after this thirty minute rest.

A final note is that samples as tested 'deteriorated' over time. We could verify this behavior by observing extensive pinning of defects on the walls. This effect became noticeable after roughly 70–150 cumulative temperature cycles of $\Delta T \approx 10$C (not counting smaller temperature cycles), and could not be effectively coun-

teracted by thorough cleaning of the sample. Because of this, the data shown were collected using different microchannels in a single sample for a complete range of T_H before it deteriorated.

2.3 Focal Conic Detection (Image Segmentation and Processing)

In order to perform reliable statistics on hundreds of collected images, we created a Python package for image processing and analysis. Individual FCDs can be detected as distinct objects and sorted by size, shape, and location in order to find large FCDs. In particular, the goal is to identify the FCDs that are located in the microchannels' pockets and occupy a large fraction of such pockets.

Smectic images were taken using brightfield microscopy at 20x magnification with a Nikon Eclipse LV100N Pol equipped with a DS-Ri2 camera. A vertical stack of images was collected to account for vertical movement due to thermal expansion of the heating stage, and the final images were chosen from this vertical stack. Although there is some subjectivity in deciding which image from a stack is most in-focus, the images that worked best for our image segmentation are those slightly (2-3μm) below the point where the image may seem in-focus. The best segmentation occurred when the boundary between FCDs is not only sharp, but also highly contrasting (darker than the surrounding region). Additionally, the numerical aperture of the objective was reduced to increase this contrast further (before post-processing).

Images were segmented in the red channel using the Photutils package of the Astropy Python library[51]. A flatfield image taken immediately before loading the sample (with the exact same brightness and magnification used throughout imaging) corrected for non-uniformity in brightness across the captured image. The contrast of the images was enhanced before segmentation (as needed) using percentile stretching of red channel intensity to make FCD boundaries more pronounced. Afterwards, images were segmented.

Segmented images were further treated in two separate ways. First, a pixel mask corresponding to the unfilled walls of the microchannel was applied to separate objects that were mistakenly detected as part of the channel wall. Secondly, small manual cuts were made to separate FCDs that were not properly separated into distinct objects (typically 2–10 instances per image). Afterwards, the image was re-segmented.

The edges of segmented objects, corresponding to FCD boundaries, were calculated. These edges were fitted with an ellipse-fitting script that estimated the shape and size of FCDs. The ellipse radius was calculated using the semi-major and semi-minor axes, and corrected with a constant factor (depending on image brightness and segmentation parameters) accounting for pixel erosion from the segmentation. The centers of the ellipses were also corrected to account for movement of the sample between successive temperature ramps occurring from slight expansion of the heating stage (up to 90μm in either axis). This correction was calculated using linear stack alignment with the SIFT plugin for FIJI (ImageJ).

3 Results

3.1 Spontaneous Large Focal Conic Domains

When cooled slowly to the smectic phase, FCDs formed in microchannels and packed as shown in Figure 1. Each microchannel wall had periodic indentations and occasionally large FCDs spontaneously filled large portions of the 36μm–wide, roughly circular "pockets" formed by the indentations, spanning the widest part of the channel. Our microchannels had variations in the geometry of these pockets. For simplicity, we varied the combination of width w and spacing s between pockets (see Figure 1), while keeping the height of the pocket at 14–15μm.

In our study, we focused only on FCDs with two distinct characteristics: they occupy a large portion of a pocket formed by the microchannels and they are centrally located inside their respective pocket. The reason for this choice is that we wanted to have a spatial reference to clearly identify and label each FCD. If one single large FCD occupies an entire channel pocket, or at least the largest fraction of it, it is easy to identify and avoids ambiguity. The variations in channel geometry greatly influenced the rate of formation of the large FCDs. Certain channel geometries led to perfect FCD arrays, with large FCDs in every pocket, while others rarely had large FCDs form at all, and other geometries featured large FCDs packed against the sides of the wall or against FCDs in neighboring pockets, distorting them. In this study, we focus only on the channel geometries that yielded a mix of well-formed large FCDs and smaller and irregularly packed FCDs.

To isolate the large and central FCDs, we analyzed FCDs using two parameters, the first parameter being the size. The size of FCDs was represented as the radius, and calculated as the average of the semi-major and semi-minor axes of fitted ellipses. The second parameter describing FCD packing was the location of FCDs relative to the center of the pockets. Specifically, this parameter was the distance from the center of a detected FCD to the center of the pocket it is closest to. The reason for this parameter is our need to distinguish two cases.

The first case is the primary focus of this paper—large, centered FCDs. In this case, their distance from the center of the pocket is much smaller than their radius (Figure 3a–b), and they are positioned in such a way that another large FCD cannot fit in the same pocket.

Large FCDs that don't meet this description often fall into other distinct categories. FCDs are sometimes sectors and tucked into the pocket indentation (Fig. 3c), pinned to the wall. A second category is that of large crescent-shaped FCDs pinned against the wall, but off-center (Fig. 3d–e; blue dashed lines). This means they are outside the pocket, either partially occupying the narrow part of the channel (Fig. 3d) or occupying a neighboring pocket (Fig. 3e). This sometimes allows another large FCD to occupy the center of the pocket (indicated with solid red lines in Fig. 3d–e). Finally, we also observed instances of multiple large off-center FCDs that partially filled opposing sides of a pocket (Fig. 3f).

These considerations allowed us to look for a method to automatically identify the large, pocket-filling FCDs. Figure 4 shows the FCD distance from pocket center plotted against the FCD radius for a particular set of data, where we labeled manually and

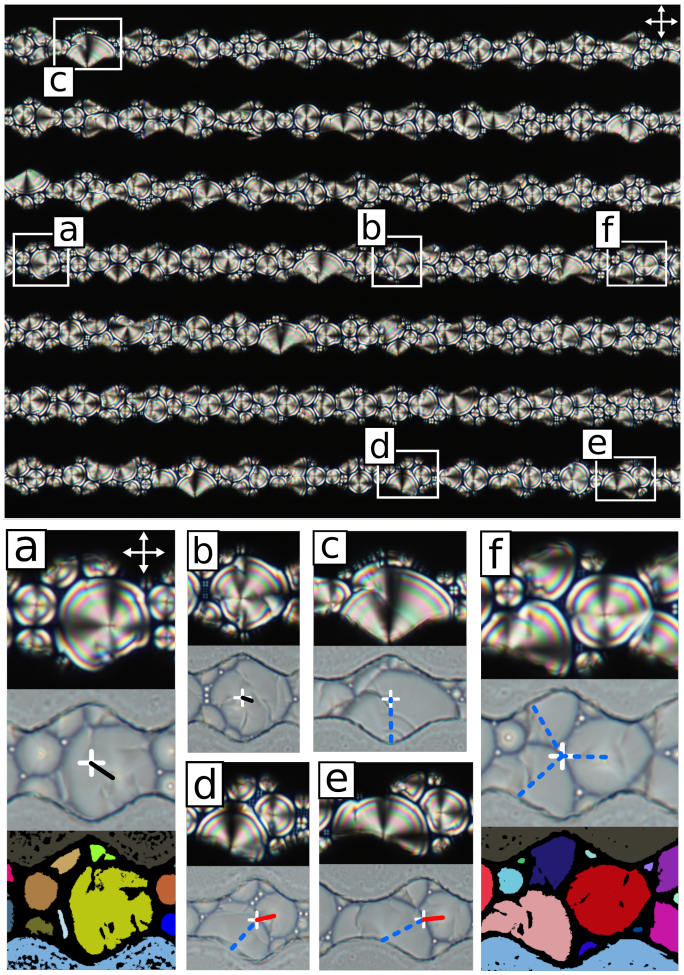

Fig. 3 Full view of microchannels taken with polarized optical microscopy (large image). Various closeup images (a–f) are shown, with a corresponding brightfield image shown below each. Corresponding segmented images are also shown for (a) and (f), which are generated using the brightfield images and are used in ellipse fitting. The white cross on each brightfield image indicates the center of the pocket, with lines drawn towards the center of the largest FCDs. The black lines (a–b) correspond to FCDs that are large and centrally located. The dashed blue and solid red lines (c–f), in contrast, indicate various situations where large FCDs are competing for the center of the pocket.

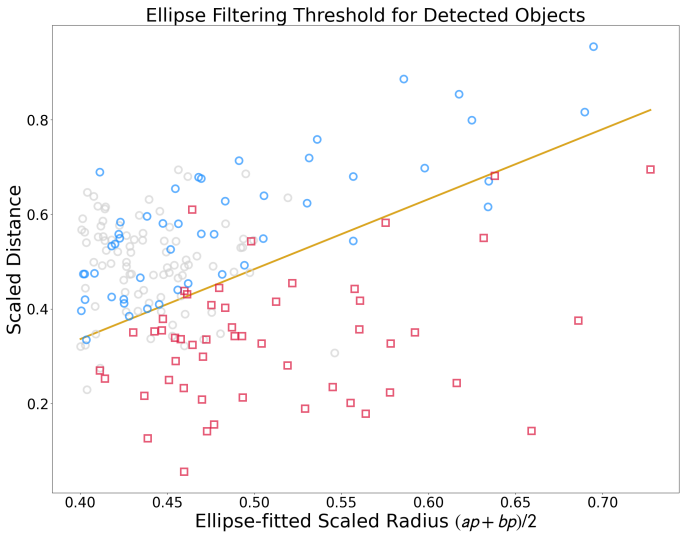

Fig. 4 Distribution of FCD size and distance from the center of their closest pockets for a set of data available online[52]. The line represents the ellipse filtering threshold for categorizing detected objects. The radii are calculated with the semi-major and semi-minor axes (ap and bp) of fitted ellipses and the distance and radii are both scaled to the width of the corresponding pocket, giving unit-less quantities. Red boxes below the line correspond to those that were marked as large and centrally located within their pockets as opposed to those that weren't (blue circles). The orange line roughly separates these data, and is used as a threshold for all other analyses. Some were not categorized (grey circles) but were included in the plot to give an overall sense of their distribution.

classified each FCD. For this particular set of data, available online[44], we manually labeled all the large and centered FCDs. The FCDs corresponding to these pockets are represented with colored markers in Figure 4, with red squares corresponding to large and centered FCDs, and blue circles corresponding to those that were not. In this figure, we only show the largest FCDs, while the full distribution is visible in Supplemental Figure S2.

After doing this manual classification, we plotted a line (orange line in Figure 4) to represent a filter used to distinguish the "accepted" FCDs from the "not-accepted" ones (the cases shown in Figure 3). This line represents a compromise between identifying all the acceptable FCDs and discarding the others. It is possible to notice that a small number of FCDs fall on the wrong side of the line, but we estimate this to be comparable with the errors one would make by manually detecting FCDs. The line in the figures represents one of the rules chosen to count the large FCDs in the following sections, the other rule being a cutoff radius equal to 0.4 times the radius of the pocket. These data allowed us to identify a range of suitable selection parameters (or filters) applied to ellipses fitted to the automatically segmented FCDs in subsequent analyses.

3.2 Measuring Geometric Memory

In order to quantify memory in our system, we chose to measure the likelihood that large, centrally located focal conic domains reappeared at their original location after the system had been heated back and forth across the smectic-A–nematic phase transition. To do this, we used a series of temperature ramps like that

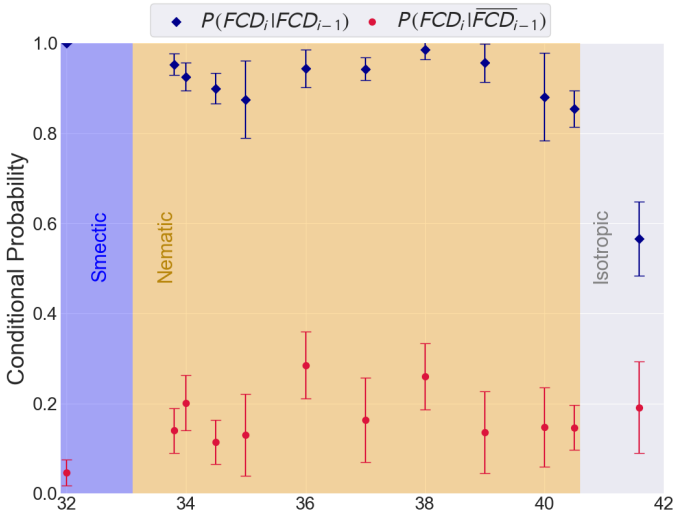

Fig. 5 Conditional Probability $P(FCD_i|FCD_{i-1})$ vs. the maximum heating temperature T_H (dark blue, upper plot) and $P(FCD_i|\overline{FCD}_{i-1})$ vs T_H (red, lower plot). Plotted values and errors represent weighted averages of different channels (a detailed description of error calculation is provided in Supplemental Materials section 1).

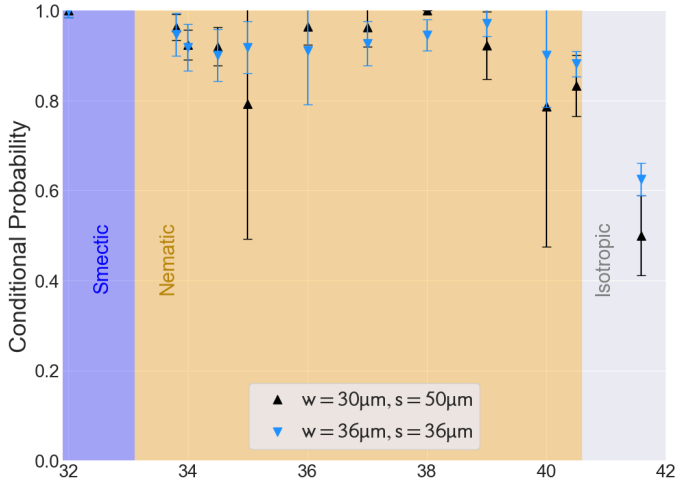

Fig. 6 Conditional Probability $P(FCD_i|FCD_{i-1})$ vs. the maximum heating temperature T_H. Different channels are grouped according to their geometry (w,s), where w and s represent pocket width and pocket spacing, respectively.

shown in Figure 2 and explained in Section 2.2, where the sample is heated to a variable temperature T_H in the nematic phase before being cooled to the smectic phase.

For each value of T_H, a conditional probability $P(FCD_i|FCD_{i-1})$ can be calculated measuring the fraction of FCDs that form in each pocket before and after heating—the conditional probability that any given FCD at heating cycle i forms at the same position as a FCD at heating cycle $i-1$. Here we count only the large FCDs we described previously (red boxes in Fig. 4). In other words, we are measuring the probability that, if a large, central FCD is formed in a pocket before the temperature ramp, a large, central FCD will form in the same pocket after the temperature ramp. This conditional probability was averaged over multiple heating cycles, averaged over different channel types, and plotted in Figure 5 (dark blue diamonds). All data are available online[44].

A small drop in $P(FCD_i|FCD_{i-1})$ is visible at lower temperatures (32–34C) after the smectic–nematic transition. The data demonstrate that the nematic phase is very capable of retaining the memory of FCD configurations throughout a large range of temperatures. This is represented by the nearly constant value of $P(FCD_i|FCD_{i-1})$ between 33C and 40C. The conditional probability is not fully reduced until the sample goes through the nematic–isotropic transition, when $P(FCD_i|FCD_{i-1})$ sharply drops to a value still larger than the background rate of FCD formation (the background rate on average ranging between 0.2 and 0.4, as shown in Supplemental Figure S3).

In order to rule out other possible effects, we also plotted $P(FCD_i|\overline{FCD}_{i-1})$ in Figure 5 (red plot), i.e. the probability that a FCD is formed in a pocket where a previous FCD was not present. If no FCD is present in a pocket before the heating/cooling cycle, we expect that the probability of forming a FCD is temperature independent, and should not significantly differ between samples heated into nematic or isotropic phase, as we indeed verify. Moreover, if the two events FCD_i and $FCD_{i-1}$are uncorrelated, from Bayes theory we expect the conditional probability to be simply equal to $P(FCD_i)$, as we can confirm (Supplemental Material Figure S3). Similarly, $P(\overline{FCD}_i|\overline{FCD}_{i-1})$, shown in Supplemental Figure S4, is independent from the heating temperature.

A dependence on temperature of $P(FCD_i|\overline{FCD}_{i-1})$ would indicate that FCDs formed at locations where there were previously none as a result of some temperature-dependent effect, such as for example an increase in FCD formation rate due to degradation of the sample leading to increased surface pinning. This was indeed the case when we collected additional data near the smectic–nematic phase transition, about 3 months after collecting the previous data (Supplemental Figure S5). Here, the probability of forming defects where there were none before increases, due most likely to the increased geometric pinning.

However the average data does not provide the full story. Measurements are grouped according to their shared variations in microchannel geometry (parameters w and s in Fig. 1), with two geometries plotted in Figure 6. The channels with w=36 and s=36 (blue) showed less variation in the conditional probability as a function of the temperature. In these channels we saw a higher tendency of FCDs to form in particular pockets (throughout multiple experiments), giving effectively a higher "background level" in the conditional probability measurement. This can be easily identified as the value of $P(FCD_i|FCD_{i-1})$ when heated to the isotropic phase, where any liquid crystal defect is erased and therefore we do not expect any thermal memory. The value $P(FCD_i|FCD_{i-1})$ therefore represents a combination of two effects—a thermal memory, which reduces as the temperature is raised, and a constant background value that depends on the morphology of the channels. In fact, the geometry of the channels greatly influences the formation rate of FCDs. For our study, we focus on channels for which large FCDs are formed in about 20-40% of the pockets. This is to avoid a too high/too low

background level for detection of FCDs. However, the formation rate alone does not tell us where exactly the FCDs will form, and in which specific pockets. This is not influenced by the channel geometry – while on the other hand it could be influenced by impurities or by irregularities on the channel surface or along the channel walls. Despite slight variations in behavior, the drops in $P(FCD_i|FCD_{i-1})$ in both geometries occur at nearly the same T_H, suggesting that indeed we are seeing a thermal memory effect, influenced by more factors than mere geometry and defect pinning.

4 Discussion and conclusions

Our results overall show that the probability that a FCD forms in the pocket of a micro-channel after a heating-cooling cycle if a FCD was present before the cycle depends on the maximum heating temperature. The biggest change happens after the nematic–isotropic phase transition has taken place. Here the "memory" has a net decrease.

We should note also that certain geometries and channels have a defect-retention effect (distinct from memory) where large 'background' value of $P(FCD_i|FCD_{i-1})$ occur—in some instances so large that $P(FCD_i|FCD_{i-1}) \approx 1$ for any temperature, even when heated to isotropic, making them unsuitable for our experiments. This can be due to two factors: either the size and shape of the channel pocket is especially favorable for the formation of large FCDs, or the channel has cracks/imperfections in microchannel walls that pin defects to the same locations and influence FCD formation. This latter hypothesis is supported by the fact that repeated heating/cooling causes sample to deteriorate, and this causes $P(FCD_i|FCD_{i-1})$ to rise over the course of months, presumably as the surface gains more imperfections. Sample deterioration is to be expected for an experiment consisting of hundreds of repeated heating/cooling cycles, which may affect the material properties, surface cracks, or chemical properties of SU8 (and LC anchoring).

Finally , these experiments have some key differences from the experiments in thin film nematics. In thin films, a direct connection between boojum defects and FCDs could be made, as these two types of defects have commonalities in their molecular alignment. Similarly, the conversion between FCDs and cholesteric defects could be mediated by a central disclination with the same winding number. However, in our experiments the channels in the nematic phase are populated by disclination lines with semi-integer winding number (Supplemental Figure S6). These disclinations move around the channels especially at high temperature. We have tried to identify a precise relation between the position of the defects in the nematic phase and the location of the large FCDs. However, our data seem to show that the FCDs do not always form in correspondence with nematic defects. We have identified a few typical cases, exemplified in Supplemental Figure S7: i) Defects that are clearly formed in correspondence of surface impurities. These are easy to identify because they do not disappear in the isotropic phase. When the system is cooled back into nematic phase, a defect pins in the same location and is preserved all the way through the smectic transition. ii) Boojum defects formed in nematic phase, which are maintained in the smectic phase as expected. This means, that converging boojums with positive topological charge become the center of FCDs, diverging boojums with positive charge become the mid-point in between multiple adjacent FCDs and boojums with negative charge become the mid-point between two adjacent FCDs. This was well characterized in ref.[19,20] However, in this case the presence of the boojum defects in nematic phase does not predict the size of FCDs. iii) In some cases, there is no visible defect in nematic phase and yet large FCDs forms in the smectic phase. Despite this, and without needing to track the movement of the nematic defects, we see a measurable amount of memory in the final FCD configurations.

In conclusion, this study attempts at providing a quantitative assessment of memory effects in liquid crystals across a phase transition. Here we focus on the smectic A-nematic phase transition, and we study LC films with hybrid alignment that form FCDs in the smectic phase and disclination lines in the nematic phase. The micro-channels with undulated boundaries provide a platform to create well-controlled defect arrays, to help isolate the relevant defects. Despite the difference in molecular alignment, we observe a measurable temperature dependence of the memory, with significant memory loss occurring at the nematic-isotropic transition.

This result opens many more questions. For example, in 8CB the elastic constants change rapidly near the isotropic phase. Further measurements with different types of liquid crystals can help elucidate whether this has an effect on how sharp the memory decreases at the phase transition.

Author Contributions

S.H. performed the experiments and analyzed the data. A. de la V. contributed to the data analysis and the segmentation protocol. F.S. and S.H. designed the experiment. F.S. provided funding.

Conflicts of interest

There are no conflicts to declare.

Acknowledgements

We thank Zhaofei Zheng and Kirsten Endresen for help with sample preparation and characterization. We thank Sreyas Chintapalli for advice with photolithography. We also thank Tim Reeder and Collin Broholm for their advice on binomial error estimation. We acknowledge funding from NSF-DMR 2004532.

Notes and references

1 V. P. Janaki, S. Moorthi and M. L. N. M. Mohan, *The European physical journal. E, Soft matter*, 2023, **46**, 38.
2 P. Bury, M. Veveričík, F. Černobila, N. Tomašovičová, V. Lacková, K. Zakutanská, M. Timko and P. Kopčanský, *Nanomaterials*, 2023, **13**, 2987.
3 A. Mouquinho, J. Figueirinhas and J. Sotomayor, *Liquid Crystals*, 2020, **47**, 636–649.
4 S. Kelly and M. O'Neill, *Handbook of Advanced Electronic and Photonic Materials and Devices*, Academic Press, Burlington, 2001, pp. 1–66.
5 M. L. N. M. Mohan, *Liquid Crystals*, 2023, **50**, 210–217.

6 A. V. Nomoev, T. A. Chimytov, S. V. Kalashnikov and D. Z. Bazarova, *AIP Conference Proceedings*, 2023, **2504**, 030075.

7 K. Zakutanská, D. Miakota, V. Lacková, S.-C. Jeng, D. Węgłowska, F. Agresti, M. Jarošová, P. Kopčanský and N. Tomašovičová, *Journal of Molecular Liquids*, 2023, **391**, 123357.

8 S. Kralj, D. Jesenek, G. Cordoyiannis, G. Lahajnar and Z. Kutnjak, *Fluid Phase Equilibria*, 2013, **351**, 87–93.

9 T. Ohzono, H. Monobe, R. Yamaguchi, Y. Shimizu and H. Yokoyama, *Applied Physics Letters*, 2009, **95**, 014101.

10 N. Aryasova, *Molecular Crystals and Liquid Crystals*, 2007, **475**, 73–83.

11 J. Jones, G. P. Bryan-Brown, E. L. Wood, A. Graham, P. Brett and J. R. Hughes, Liquid Crystal Materials, Devices, and Flat Panel Displays, 2000, pp. 84–93.

12 C. P. Chen and C. G. Jhun, *Sensors*, 2020, **20**, 5937.

13 F. Serra, S. M. Eaton, R. Cerbino, M. Buscaglia, G. Cerullo, R. Osellame and T. Bellini, *Advanced Functional Materials*, 2013, **23**, 3990–3994.

14 F. Serra, M. Buscaglia and T. Bellini, *Materials Today*, 2011, **14**, 488–494.

15 Y. Shoji, M. Kobayashi, A. Kosaka, R. Haruki, R. Kumai, S.-i. Adachi, T. Kajitani and T. Fukushima, *Chem. Sci.*, 2022, **13**, 9891–9901.

16 T. Araki, M. Buscaglia, T. Bellini and H. Tanaka, *Nature materials*, 2011, **10 4**, 303–9.

17 I. Muševič and S. Žumer, *Nature materials*, 2011, **10 4**, 266–8.

18 M. R. Nejad, A. Doostmohammadi and J. M. Yeomans, *Soft Matter*, 2021, **17**, 2500–2511.

19 A. Suh, M.-J. Gim, D. Beller and D. K. Yoon, *Soft Matter*, 2019, **15**, 5835–5841.

20 M. Gim, D. A. Beller and D. K. Yoon, *Nature Communications*, 2017, **8**, 15453.

21 S. M. Hare, B. Lunsford-Poe, M. Kim and F. Serra, *Materials*, 2020, **13**, 3761.

22 M. Kleman and O. D. Lavrentovich, *Liq. Cryst.*, 2009, **36**, 1085–1099.

23 Y. H. Kim, D. K. Yoon, M. C. Choi, H. S. Jeong, M. W. Kim, O. D. Lavrentovich and H.-T. Jung, *Langmuir*, 2009, **25**, 1685–1691.

24 D. S. Kim and D. K. Yoon, *Journal of Information Display*, 2018, **19**, 7–23.

25 Y. H. Kim, D. K. Yoon, H. S. Jeong and H.-T. Jung, *Soft Matter*, 2010, **6**, 1426–1431.

26 Y. Xia, A. Honglawan and S. Yang, *Liquid Crystals Reviews*, 2019, **7**, 30–59.

27 S.-B. Wu, J.-B. Wu, H.-M. Cao, Y.-Q. Lu and W. Hu, *Phys. Rev. Lett.*, 2023, **130**, 078101.

28 R. S. Preusse, E. R. George, S. A. Aghvami, T. M. Otchy and M. A. Gharbi, *Soft Matter*, 2020, **16**, 8352–8358.

29 W.-S. Wei, J. Jeong, P. J. Collings and A. G. Yodh, *Soft Matter*, 2022, **18**, 4360–4371.

30 F. Serra, M. A. Gharbi, Y. Luo, I. B. Liu, N. D. Bade, R. D. Kamien and K. J. Stebe, *Advanced Optical Materials*, 2015, **3**, 1287–1282.

31 A. Honglawan, D. A. Beller, M. Cavallaro, R. D. Kamien, K. J. Stebe and S. Yang, *Proceedings of the National Academy of Sciences*, 2013, **110**, 34–39.

32 Y. H. Kim, D. K. Yoon, H. S. Jeong, O. D. Lavrentovich and H.-T. Jung, *Advanced Functional Materials*, 2011, **21**, 610–627.

33 J.-B. Wu, S.-B. Wu, H.-M. Cao, Q.-M. Chen, Y.-Q. Lu and W. Hu, *Advanced Optical Materials*, 2022, **10**, 2201015.

34 S.-P. Do, A. Missaoui, A. Coati, D. Coursault, H. Jeridi, A. Resta, N. Goubet, M. M. Wojcik, A. Choux, S. Royer, E. Briand, B. Donnio, J. L. Gallani, B. Pansu, E. Lhuillier, Y. Garreau, D. Babonneau, M. Goldmann, D. Constantin, B. Gallas, B. Croset and E. Lacaze, *Nano Letters*, 2020, **20**, 1598–1606.

35 M. A. Gharbi, D. A. Beller, N. Sharifi-Mood, R. Gupta, R. D. Kamien, S. Yang and K. J. Stebe, *Langmuir*, 2018, **34**, 2006–2013.

36 A. Honglawan, D. S. Kim, D. A. Beller, D. K. Yoon, M. A. Gharbi, K. J. Stebe, R. D. Kamien and S. Yang, *Soft Matter*, 2015, **11**, 7367–7375.

37 R. Pratibha, W. Park and I. I. Smalyukh, *Journal of Applied Physics*, 2010, **107**, 063511.

38 M. Walters, Q. Wei and J. Z. Y. Chen, *Phys. Rev. E*, 2019, **99**, 062701.

39 A. Piven, D. Darmoroz, E. Skorb and T. Orlova, *Soft Matter*, 2024, **20**, 1380–1391.

40 E. N. Minor, S. D. Howard, A. A. S. Green, M. A. Glaser, C. S. Park and N. A. Clark, *Soft Matter*, 2020, **16**, 1751–1759.

41 R. A. Chowdhury, A. A. S. Green, C. S. Park, J. E. Maclennan and N. A. Clark, *Phys. Rev. E*, 2023, **107**, 044701.

42 Y. Li, Z. Zarei, P. N. Tran, Y. Wang, A. Baskaran, S. Fraden, M. F. Hagan and P. Hong, *Soft Matter*, 2024, **20**, 1869–1883.

43 H. Ren, W. Wang, W. Tang and R. Zhang, *Phys. Rev. Res.*, 2024, **6**, 013259.

44 E. Hedlund, K. Hedlund, A. Green, R. Chowdhury, C. S. ark, J. E. Maclennan and N. A. Clark, *Physics of Fluids*, 2022, **34**, 103608.

45 A. Killeen, T. Bertrand and C. F. Lee, *Biophysical Reports*, 2024, **4**, 100142.

46 I. Dierking, J. Dominguez, J. Harbon and J. Heaton, *Liquid Crystals*, 2023, **50**, 1461–1477.

47 R. Betts and I. Dierking, *Soft Matter*, 2023, **19**, 7502–7512.

48 N. Osiecka-Drewniak, Z. Galewski and E. Juszyńska-Gałązka, *Crystals*, 2023, **13**, 1187.

49 M. Masias, J. Freixenet, X. Lladó and M. Peracaula, , 2012, **422**, 1674–1689.

50 Kayaku Advanced Materials, *SU-8 2000, 2000.5-2015 Technical Data Sheet,*, ver. 1 edn, 2020.

51 L. Bradley, B. Sipőcz, T. Robitaille, E. Tollerud, Z. Vinícius, C. Deil, K. Barbary, T. J. Wilson, I. Busko, A. Donath, H. M. Günther, M. Cara, P. L. Lim, S. Meßlinger, S. Conseil, A. Bostroem, M. Droettboom, E. M. Bray, L. A. Bratholm, G. Barentsen, M. Craig, S. Rathi, S. Pascual, G. Perren, I. Y. Georgiev, M. de Val-Borro, W. Kerzendorf, Y. P. Bach, B. Quint

and H. Souchereau, *astropy/photutils: 1.8.0*, 2023, https://doi.org/10.5281/zenodo.7946442.

52 S. Hare and F. Serra, *Additional files and raw data available*, https://github.com/fraserrasdu/SoftMatter_Hare, 2025.

Data Availability Statement

Data for this article, including original microscopy images, processed images and numerical tables, are available either in Supplemental Materials or in the online repository at this address: https://github.com/fraserrasdu/SoftMatter_Hare.